CHROMOSPHERIC THERMODYNAMIC CONDITIONS FROM INVERSIONS OF COMPLEX Mg II h&k PROFILES OBSERVED IN FLARES

Alberto Sainz Dalda[1, 2] and Bart De Pontieu[1, 3, 4]

[1]*Lockheed Martin Solar & Astrophysics Laboratory, 3251 Hanover Street, Palo Alto, CA 94304, USA*
[2]*Bay Area Environmental Research Institute, NASA Research Park, Moffett Field, CA 94035, USA.*
[3]*Rosseland Center for Solar Physics, University of Oslo, P.O. Box 1029 Blindern, NO-0315 Oslo, Norway*
[4]*Institute of Theoretical Astrophysics, University of Oslo, P.O. Box 1029 Blindern, NO-0315 Oslo, Norway*

ABSTRACT

The flare activity of the Sun has been studied for decades, using both space- and ground-based telescopes. The former have mainly focused on the corona, while the latter have mostly been used to investigate the conditions in the chromosphere and photosphere. The Interface Region Imaging Spectrograph (IRIS) instrument has served as a gateway between these two cases, given its capability to observe quasi-simultaneously the corona, the transition region, and the chromosphere using different spectral lines in the near- and far-ultraviolet ranges. IRIS thus provides unique diagnostics to investigate the thermodynamics of flares in the solar atmosphere.

In particular, the Mg II h&k and Mg II UV triplet lines provide key information about the thermodynamics of low to upper chromosphere, while the C II 1334 & 1335 Å lines cover the upper-chromosphere and low transition region. The Mg II h&k and Mg II UV triplet lines show a peculiar, pointy shape before and during the flare activity. The physical interpretation, i.e., the physical conditions in the chromosphere, that can explain these profiles has remained elusive. Several numerical experiments with forward modeling or ad-hoc assumptions have partially succeeded in reproducing these profiles, although the derived thermodynamic parameters seem either unrealistic or difficult to interpret in terms of physical mechanisms.

In this paper, we show the results of a non-LTE inversion of such peculiar profiles. To better constrain the atmospheric conditions, the Mg II h&k lines and the Mg II UV triplet lines are simultaneously inverted with the C II 1334 & 1335 Å lines. This combined inversion leads to more accurate derived thermodynamic parameters, especially the temperature and the turbulent motions (micro-turbulence velocity). We use an iterative process that looks for the best fit between the observed profile and a synthetic profile obtained by considering non-local thermodynamic equilibrium and partial frequency redistribution of the radiation due to scattered photons. This method is computationally rather expensive ($\approx 6\,CPU-hour/profile$). Therefore, we use the k-means clustering technique to identify representative profiles and associated representative model atmospheres. By inverting the representative profiles with the most advanced inversion code (STiC), we are able to conclude that these unique, pointy profiles are associated with a simultaneous increase of the temperature and the electron density in the chromosphere, while the micro-turbulence velocity has values between 5-15 km/s, which seem to be more realistic values than the ones suggested in previous work. More importantly, the line-of-sight velocity shows a large gradient along the optical depth in the high chromosphere. This seems to be the parameter that gives the pointy aspect to these profiles.

Keywords: Sun, chromosphere, flares, thermodynamics, inversions

Corresponding author: Alberto Sainz Dalda
sainzdalda@baeri.org
asainz.solarphysics@gmail.com

1. INTRODUCTION

A flare is the release of magnetic energy as a consequence of reconnection in magnetically stressed coronal loops. The magnetic energy stored in these loops comes from the low solar atmosphere. Once it is released, it is transferred to both the outer and the lower solar atmosphere in a variety of energy forms: radiation, thermal energy, non-thermal energy (accelerated particles and turbulence), kinetic energy, large-scale Alfvén waves, and others. The most evident observational counterpart of this sudden release of energy is an enhancement in radiation flux (intensity) in almost any spectral range. This description, although simplistic, allow us to picture the basic flare phenomena. Many complex physical processes however occur and need to be properly studied for a full understanding of this type of solar event. This complexity is also reflected in the observational data we have of flares.

In the last few decades, with the advance of instrumentation, especially instrumentation onboard space-based observatories, we have largely improved our access to a steady flow of high-quality flare data. In this paper, we focus our attention on the interpretation of spectral signatures in the Mg II h&k and C II 1334 & 1335 Å lines observed by the Interface Region Imaging Spectrograph (IRIS, De Pontieu et al. (2014)) during the X1.0-class flare of SOL2014-03-29T17:48. In particular, we will analyze the profiles in these lines corresponding to the flare ribbons duding the maximum of the flare. In this location, at that time, the Mg II h&k profiles are characterized by a pointy, broad-on-the-base shape[1]. Figure 1 shows a typical Mg II h&k profile in the quiet Sun. The main features of the lines and their rest wavelength positions are indicated by labels and vertical lines respectively.

The resonance Mg II h&k profiles have been used in the past for the study of the chromosphere (Lemaire and Skumanich 1973; Kohl and Parkinson 1976; Kneer et al. 1981; Lites and Skumanich 1982), including the study of flares (Lemaire et al. 1984). The theoretical modeling and interpretation of these lines have been an active topic for decades (e.g., Feldman and Doschek 1977; Lites and Skumanich 1982; Lemaire and Gouttebroze 1983; Uitenbroek 1997). More recently, thanks to the advance in the computational resources and triggered by the huge amount of data provided by IRIS, these lines have been investigated using more realistic assumptions when solving the radiative transfer equation (RTE) (e.g., Leenaarts et al. 2013b,a; Pereira et al. 2013, 2015; Sukhorukov and Leenaarts 2017), including treatment
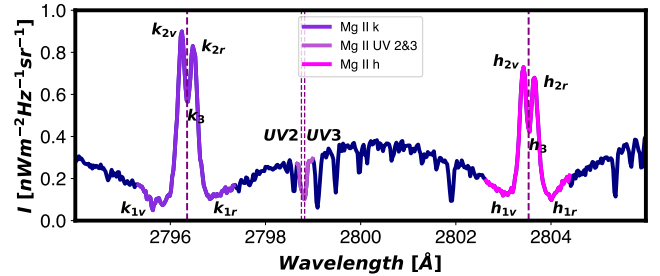
Figure 1. Mg II h&k and Mg II UV2&3 lines - the latter belonging to the Mg II UV triplet - as observed by IRIS in the quiet-sun. Spectral sampling is 0.025. The rest position for the core of the lines is indicated by the vertical dashed lines. The main features of the h and k lines are indicated with labels. The wavelength values are given in vacuum.

of polarized radiation (del Pino Alemán et al. 2016; Manso Sainz et al. 2019).

In the *extreme* and *very pointy* profiles (see, e.g, Fig. 3) studied in this investigation, the depression (or self-reversal) in the core of the line (k_3 and h_3) has disappeared and the top of the profiles is defined by an inverted-V shape in just a few spectral samples. Note that some authors refer to *single-peaked* Mg II h&k profiles as those profiles that show k_3 and h_3 in emission, but at the same intensity or slightly higher or lower than the k_2 and h_2 spectral features. Such profiles, while being single-peaked, are mostly characterized by being *flat-topped*, as they were described by Carlsson et al. (2015). In contrast, the Mg II h&k profiles discussed in this paper are *single-peaked* as well, but their main characteristics are: i) their very pointy top, as a consequence of the lack of k_3 and h_3 features and of having the violet and red components of the k_2 and h_2 almost totally blended in one pointy feature, ii) extended broad wings, which renders indistinguishable the k_1 and/or h_1 spectral features; and iii) the subordinated Mg II UV triplet lines are in emission, in many cases also showing a pointy, broad shape, albeit not as extremely pointy, since the top of these lines shows an inverted-U shape.

The C II 1334 & 1335 Å lines also show a pointy shape, and in many cases it is red-shifted or showing a strong red-shifted component. Rathore et al. (2015) investigated the behavior of C II 1334 & 1335 Å lines in quiet Sun and found that the intensity profile may have both an optically thick and an optical thin component. These authors found, also through the analysis of the ratio of the intensity of the C II 1334 & 1335 Å lines, that the single-peak profiles of C II 1335 Å formed higher in the atmosphere than the single-peak profiles C II 1334 Å.

These kind of pointy spectral line profiles, specially the Mg II h&k, were identified in IRIS data as soon as the instrument started to observe flares. Kerr et al. (2015) reported strong emission in the Mg II h&k and the Mg II UV2&3 lines in the

---

[1] By shape of a profile or a line, we mean the spectral distribution of the intensity (specifically, the spectral radiance) with respect to the wavelength in a given spectral range.

ribbons of the M class flare SOL2014-02-13T01:40 observed by IRIS. The authors noted the absence of the depression in the core of the Mg II h&k lines, i.e., the lack of the k_3 and h_3 features. They also concluded, based on the ratio of the intensity between the k and the h lines, that these lines are optically thick during the flare. As we just mentioned above, this may not be the case for the C II 1334 & 1335 Å lines. The profiles shown by Kerr et al. (2015) are inverted-U pointy profiles. Figure 6 of Liu et al. (2015) shows a selection of Mg II h&k profiles belonging to the flare studied in the current paper. As we will discuss later, some of the profiles shown in that figure are *very pointy* profiles, while the ones shown in Figure 10 of that paper are *extremely pointy* profiles or type A or B (see below). Xu et al. (2016) identified *extremely pointy* Mg II h&k and C II 1334 & 1335 Å profiles in the positive polarity part of the ribbon of the M1.4-class SOL2013-08-17T18:43 flare, but not in the negative polarity part (decrease in the contrast of the intensity).

Several models have been proposed to explain the pointy profiles, particularly the ones observed by IRIS on SOL2014-03-29T17:48. Rubio da Costa et al. (2016); Rubio da Costa and Kleint (2017) studied the parameters needed to model the Mg II h&k profiles observed during the maximum of this flare. The authors modified the thermodynamics parameters in hydrodynamic simulations (RADYN, Carlsson and Stein 1995, 1997), and then they obtained the synthetic profiles of these lines using the RH code Uitenbroek (1997) considering non-local thermodynamic equilibrium (non-LTE) and partial frequency redistribution of the scattered photons. The authors obtained inverted-U, single Mg II h&k profiles by increasing the temperature and density in the formation region of these lines. However, the intensity of these profiles is larger than the intensity in the observed profiles. They were only able to match intensity profiles with inverted-U, single peak profiles when they considered a strong gradient in the line-of-sight velocity (v_{los}). These calculated profiles show however a significant asymmetry. In addition, their calculated profiles were not able to properly reproduce the large broad wings observed in the IRIS observations, except when they introduced micro-turbulent velocities (v_{mic}) values as large as 40 $km\ s^{-1}$, which they considered to be an unrealistic value. Zhu et al. (2019) followed a similar approach to that of Rubio da Costa et al. (2016), i.e., forward modeling using RADYN and RH, to interpret the Mg II h&k lines of the same flare studied by Rubio da Costa et al. (2016); Rubio da Costa and Kleint (2017) and by us in the current paper. In this case, the authors considered the impact of the Stark effect on line broadening. They used the STARK-B database - in which line broadening is calculated based on a semi-classical impact-perturbation theory Dimitrijević and Sahal-Bréchot (1995, 1998) - for the treatment of the quadratic Stark effect by RH. This is because the Stark effect previously im-

plemented in RH considers the adiabatic approximation to calculate the quadratic Stark effect, and this approximation may underestimate the broadening for the Mg II h&k lines during flares (Rubio da Costa and Kleint 2017). In summary, Zhu et al. (2019) were able to fit the extremely pointy Mg II h&k profiles observed by IRIS in the flare but only by considering an ad-hoc contribution of 30 times of the quadratic Stark effect obtained by using STARK-B in RH. This ad-hoc assumption allowed them to fit both the inverted-V, single peak, the intensity, and the broad wings. However, the authors were unable to provide a physical justification for the large ad-hoc enhancement of the Stark effect. They also tried to fit the broad wings by considering the STARK-B database value and various values of v_{turb}. They found an unrealistic value of $v_{turb} \approx 30\ km\ s^{-1}$ below the formation region of the line core of the Mg II h&k lines, and even in this case, the fit in the part of the wings furthest from line core is not good both for Mg II h&k and the Mg II UV triplet. In this paper, we focus our attention on the study of both the extremely pointy and the very pointy profiles observed by IRIS during the maximum of the flare. This kind of profile is mostly present during the maximum of the flare. We note that while single-peaked profiles can also be seen in the pre-flare stage and they may help us to predict the flare onset with about 30-50 minutes advance notice (Panos et al. 2018; Woods et al. 2021), these are quite different: the peak of the latter Mg II h&k profiles shows an inverted-U shape, the Mg II UV triplet is barely in emission, and the C II 1334 & 1335 Å lines show a wide inverted-U shape. The thermodynamics along the optical depth of these unique pre-flare profiles was for the first time described by Woods et al. (2021). In contrast, in the current paper we will reveal the thermodynamics of the most intriguing and peculiar profiles emitted at the maximum of the flare.

The interpretation of these extremely pointy profiles during the maximum of flares has presented a challenge for modelers and observers. In this paper, we present a solution - in good agreement with several possibilities speculated in previous work - that is able to reproduce these complex profiles. This solution provides reasonable values of the thermodynamics parameters involved in the problem, i.e., gives a realistic view of the conditions in the chromosphere of flare during its maximum.

2. MATERIALS AND METHODS

The data analyzed in this paper correspond to the maximum of the X1-class flare at SOL2014-03-29T17:48. This data are part of the multi-instrument observations that we led from the Dunn Solar Telescope at Sacramento Peak Observatory in coordination with IRIS and Hinode (Kosugi et al. 2007). Moreover, this flare was simultaneously observed by other observatories such as the *Reuven Ramaty High-Energy*
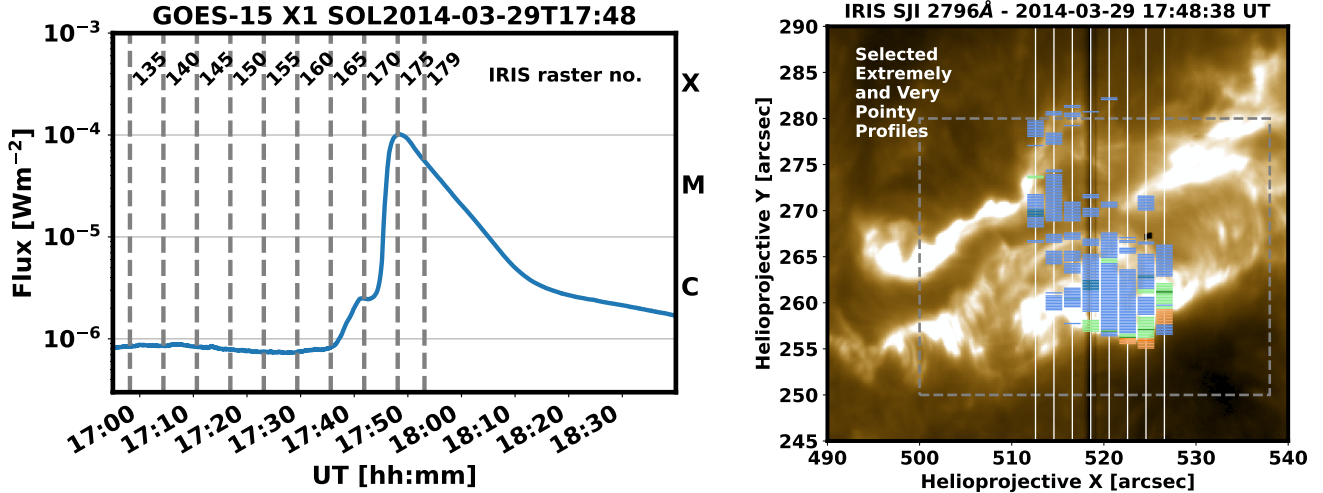
Figure 2. Left: Temporal evolution of the X-ray flux during the X1-class flare at SOL2014-04-29T17:48. The vertical lines indicate the number of some IRIS rasters that recorded this flare. Right: The image taken by the SJI instrument at IRIS during the maximum of the X1-class flare SOL2014-03-20T17:48 at 2796, that corresponds to the chromosphere. The time indicated at the top of the panel corresponds to the step number 4 of the raster. The location of the slits of all the steps of this raster (no. 175) are indicated with vertical lines. The colored squares mark the location of the extremely pointy profiles of the type A (blue) and the type B (orange), and of the very pointy or combined profiles (green). The locations in dark colors correspond to the profiles shown in figures 3, 4 and 5 respectively. The grey rectangle delimits the area shown in figure 12.

Solar Spectroscopic Imager (RHESSI, Lin et al. 2002), the *Solar Dynamics Observatory* (SDO, Pesnell et al. 2012), and the *Solar Terrestrial Relations Observatory* (STEREO, Kaiser et al. 2008). A description of this unique observation and the evolution of the flare is provided in Kleint et al. (2015).

The rasters obtained by IRIS of the region where this flare ocurred - NOAA AR 12017 - span from 2014-03-29T14:09:39 UT to 2014-03-29T17:54:16 UT. This active region was located at $\mu = 0.78$, with $\mu = cos\theta$, and θ the heliocentric viewing angle. The maximum X-ray flux measured by GOES-15 during the flare took place at 2014-03-29T17:48, which corresponds to raster no. 175 of the series of rasters taken by IRIS (see Figure 2). Each raster consisted of an 8-step scan with the slit crossing the two ribbons of the flare. Each step of the raster is $2''$ in the direction perpendicular to the slit, covering a field-of-view (FoV) of $14'' \times 174''$, with $174''$ the length of the slit. The exposure time was nominally $8s$ (but was reduced during the flare in response to the onboard automatic exposure control algorithm), the spectral sampling was 0.025 (in the NUV passband), and the spatial sampling along the slit was $0''.16$. At each step of the raster the IRIS Slit-jaw Imager (SJI) took an image. In this observation, during the acquisition at steps number 1, 5, and 7 the SJI took an image at 1400, at step number 3 an image at 2832, and steps number 2, 4, 6 and 8 images at 2796. The FoV covered by the SJI was $167'' \times 174''$. The right panel in Figure

2 shows the SJI image taken by IRIS during the maximum of the flare at 2796.

Since we are mostly interested in understanding, as accurately as possibly, the thermodynamics in the chromosphere, we decided to investigate simultaneously the C II 1334 & 1335 Å and the Mg II h&k lines. It has been shown that these lines are sensitive to thermodynamics in roughly the same region of the chromosphere, both by solving the radiative transfer equation in 3D magnetohydrodynamics models (Rathore et al. 2015), and by looking into the *mutual information* shared by these lines (Panos et al. 2021). Having this simultaneous information is a great advantage to decouple the T and v_{turb} encoded in the width of the spectral lines (see Section 4.6 in Jefferies 1968).

In this paper we proceed in a similar fashion as Woods et al. (2021) and invert simultaneously the C II 1334 & 1335 Å lines, the Mg II h&k lines, and the blended Mg II UV2&3 line. In addition, in this paper, we invert the other line of the triplet, Mg II UV1. Thus, following the analysis made by Pereira and Uitenbroek (2015) and Pereira et al. (2015) on the formation region of the Mg II h&k and the Mg II UV triplet respectively, and by Rathore et al. (2015) on the C II 1334 & 1335 Å lines, we are in principle sampling the solar atmosphere from the low chromosphere to the top of the chromosphere. The caveat here is that some of the previous work focused on quiet Sun, and it is known that during flares the line formation can sometimes be significantly different.

2.1. *Data treatment: Clustering and Inversions*

To simultaneously invert these lines we have taken advantage of the capabilities of the *STockholm inversion Code* (STiC, de la Cruz Rodríguez et al. 2016, 2019) to solve the radiative transfer equation for multiple lines and multiple atoms, considering non-local thermodynamic equilibrium and partial frequency redistribution of the radiation of the scattered photons. STiC uses the RH code Uitenbroek (2001) at the back-end to solve the RTE. STiC is the only code with the ability to properly treat the Mg II h&k, Mg II UV triplet, and C II 1334 & 1335 Å lines to recover the thermodynamics encoded in these lines. However, to invert a single *joint profile* of these lines takes between 6 to 8 *CPU − hour* - depending of the complexity of the profiles. Because of this computational burden, we have followed the strategy introduced by Sainz Dalda et al. (2019), i.e., to invert the *Representative Profile* (RP) and recover its corresponding *Representative Model Atmosphere* (RMA) by the inversion of the former. The RP is the averaged profile of a cluster of profiles that share the same shape, i.e. the same atmospheric conditions, since the shape of a profile is an encoded representation of the conditions of the matter and the radiation in the region where the lines are formed. To cluster the profiles we use the $k − means$ technique (Steinhaus 1957; MacQueen 1967). This technique, due to its simplicity and robustness, has become very popular in Machine Learning, and more recently in solar physics. However, clustering in solar data (Stokes V profiles) was already used in 2000 by (Sánchez Almeida and Lites 2000). Just like with any other method, care has to be taken when applying it to the data. It is important to understand how the method works. The core of the code is to find the centroids of clusters of elements so that the elements within a cluster are closer to its centroid than to any other centroid. For that, the code calculates the Euclidean distance (in the original $k − means$ version) between an initial number of elements randomly selected (in the original $k − means$ version) and all the elements in the data set. Then, all the closest elements to a centroid form a cluster. A new centroid is calculated as the average of all the elements of that cluster. And again, the distance between all the elements in the data set and the centroids is calculated, and new centroids are calculated as the average of the new cluster. This process is repeated until the total sum of squared distance between the within-cluster samples and their corresponding centroid is minimized, that is:

$$arg\ min_{\{C_i\}_1^K} \sum_{i=1}^{K} \sum_{x_j \in C_i} ||x_j - \mu_i||_2^2 \qquad (1)$$

with $||\cdot||_2$ the ℓ_2 norm, $\{C_i\}_1^K$ is a set of K clusters C, x_j the jth sample belonging to the ith cluster C_i, and μ_i the average of the samples x belonging to the cluster C_i, i.e., the

centroid. One of the challenges of this method is how to determine the number of clusters K that are needed to properly cluster the data set. Several methods have been proposed to minimize the impact of this choice on the resulting clustering. We have selected the *elbow method* (Thorndike 1953) to determine this number. It has been shown that a number of clusters larger than 100 is typically enough to cluster properly, in general, for IRIS Mg II h&k data sets (see Section 1.2 of *IRIS*[2] tutorial web page[2]). Based on the results of the elbow plot[3], we have decided to cluster our data set in 320 RPs. Thus, we optimize the representation of the data taking into account our computational resources (320 CPU cores). Note that what we call RPs are the centroids of the clusters of our data. In our case, a sample of our data set is the *joint profile* created by concatenating the profile of the C II 1334 & 1335 Å lines with those of the Mg II UV1line, and of the Mg II h&k lines (including the Mg II UV2&3 blended line). In machine learning jargon, the *dimensionality* of a sample is the number of features in the sample. In our case, the features are the intensity (radiative flux) at the sampled wavelengths. Therefore, the dimensionality of our data set is the number of sampled wavelengths, and the number of samples is the number of spatial pixels where these profiles were simultaneously recorded. The latter is, for our data, the common, co-aligned area recorded by IRIS in its far-ultraviolet (FUV) and the near-utraviolet (NUV) detectors. For the case studied here, the number of samples is ≈8,000 *px* per raster. Hence, to invert that number of profiles with STiC would take at least ≈ 48,000 *CPU − hours*. Nowadays, this number is not too large in terms of computation time. It would however turn computationally expensive if we wanted to invert the 175 available rasters of this flare (≈ 8.4 *MCPU − hour*). Fortunately we can reduce these numbers very significantly through the use of representative profiles. As mentioned, a number of 320 RPs per raster is enough to cluster this kind of data, and they can be inverted with a mid-size server (≈ 1050 *CPU − hour* for the 175 rasters).

Another challenge of the $k − means$ method is related with the metric used to cluster. The Euclidean distance is not the best metric when the elements or samples of the data set have a large dimensionality. In our case, the dimensionality is 624, corresponding to 116, 36, and 472 sampled wavelengths for the C II 1334 & 1335 Å, Mg II UV1, and Mg II h&k lines respectively. A reduction of the dimension of the profiles, e.g. using *Principal Components Analysis*, before clustering may mitigate this problem. In the test we have run, the effect of reducing the dimensionality before clustering has a negligible impact. This is probably because, despite having

---

[2] https://iris.lmsal.com/iris2/iris2_chapter01.html#limitations-of-iris2-inversions.

[3] https://www.youtube.com/watch?v=55sT144u5ag

a large dimension, the values of the features of our profiles are restricted to a small range of values.That means, for a given wavelength, the values of the intensity are in a well-defined and rather restricted range. As a consequence, the samples of our date set are located in a more or less well-defined region of the hyper-space defined by all ranges of all the features. However, we did adopt another approach to reduce the dimensionality. We have cropped the data around the lines, considering a spectral range large enough to capture both large blue and red shifts, eliminating the spectral positions that we are not interested in - basically those in the photospheric bump between the k and h lines. Note that we do include the Mg II UV2&3, and some wavelengths in the far wings.

Another issue of working with Euclidean distance is the scale of the features. If some features have very large values with respect to others, the smaller values will have a small impact on or significance in the distance. One way to solve this situation is to normalize each feature, for instance between 0 and 1. This is what we did for the cropped, joint profiles. These are the profiles that we have clustered. In this way, we give equal weight to all the involved spectral lines. After the $k-means$ is run over this new data set of joint profiles, the elements of a cluster are identified, that is, they are labeled with the number corresponding to that cluster. Finally, the RP of that cluster is calculated as the average of the original, joint profiles within the cluster.

This would be the standard way to proceed. But it is not the procedure we followed. During the maximum of the flare, the ratio between the maximum intensity in the Mg II h&k lines and the C II 1334 & 1335 Å lines varies from ∼100 in the pseudo-quiet-sun (the closest area to the quiet in the FoV of our data) to just ∼10 in the ribbons. A significant variation also exists between the ratio of the integrated intensity of the Mg II UV triplet lines and the Mg II h&k although not as large. This is not important for clustering the data, since, as we mentioned above, we scale all the features between 0 and 1, but it represents a problem for the inversion. STiC tries iteratively to minimize the Euclidean distance between a synthetic profile - resulting from the synthesis of a model atmosphere- and the observed profile, slightly modifying the model atmosphere at each iteration. Again, since we are using the Euclidean distance as metric, we will have a problem if the scales of the features are very different. But now, due to a coding practicality, we cannot scale the profiles individually. In this case, we use a set of weights at the sample wavelengths to scale all the profiles. These weighted profiles are then inverted. It is usual to weight the spectral range corresponding to a line with respect other line, or in the case of spectropolarimetric profiles to scale the Stokes Q, U, and V profiles with respect to I, e.g. $w_I : w_Q : w_U : w_V$=1:50:50:10. In our case, we weight the C II 1334 & 1335 Å lines, Mg

No. Cycle	1	2	3	4
T	4	7	9	13
v_{turb}	2	4	8	13
v_{los}	2	4	8	13

Table 1. Number of nodes at each cycle for the thermodynamics variables considered during the inversions.

II UV triplet lines with respect to Mg II h&k lines. However, given the large variation in the ratio of the integrated intensity of C II 1334 & 1335 Å lines with respect to the Mg II h&k lines, we decide to stratify the data in 8 percentiles, with the 8 parts dividing the number density distribution. The 3 or 4 first portions have many original profiles, representing the pseudo-quiet-sun (the closest region to the quiet-sun in the field of view). Then, the rest of the portions are associated with the flare ribbons. Each of these portions have their own weight ratio $w_{MgIIh\&k} : w_{CII} : w_{MgIIUVtriplet}$. Once the portions are defined, 40 RPs are calculated following the procedure explained above: creation of joint, concatenated profile, scaling between 0 to 1, k-means calculation, rebuild the k-means with the original data. Then, the 40 RPs of each portion are inverted considering their chosen weights. Note that in the first portions, since they are the most populated ones, the RPs are clustering a large number of profiles, while the rest of portions are clustering a significantly smaller number of profiles. This is beneficial to our investigation, since we will have a better representation by the RPs of the original profiles in the flaring areas. At this point, the data are ready to be inverted. Table 1 shows the number of nodes for each cycle considered during the inversions.

2.2. *Selected pointy profiles*

The selection of the "extremely" pointy profiles and the "very" pointy profiles was made through visual inspection. Thanks to the clustering of the data, this task is easily doable: we look for these peculiar profiles in a set of 320 RPs instead of ≈8,000 profiles. We have selected the most clear cases of these profiles to show their main characteristics. We can distinguish two main groups among the extremely pointy profiles that we have classified as Type A and Type B (see Figures 3 and 4). The core of the Mg II h&k extremely pointy profiles Type A resembles the core of a Lorenztian distribution, while the wings look like the wings of a Laplacian distribution. The C II 1334 & 1335 Å lines are pointy, redshifted, and in most of the cases their shape shows a negative skew. In some cases, the C II 1334 & 1335 Å lines saturate the response of the detector.

The Mg II h&k extremely pointy profiles type B (see Fig. 4), in addition to having the pointy core, show very enhanced wings. Sometimes, the blue wing is slightly more
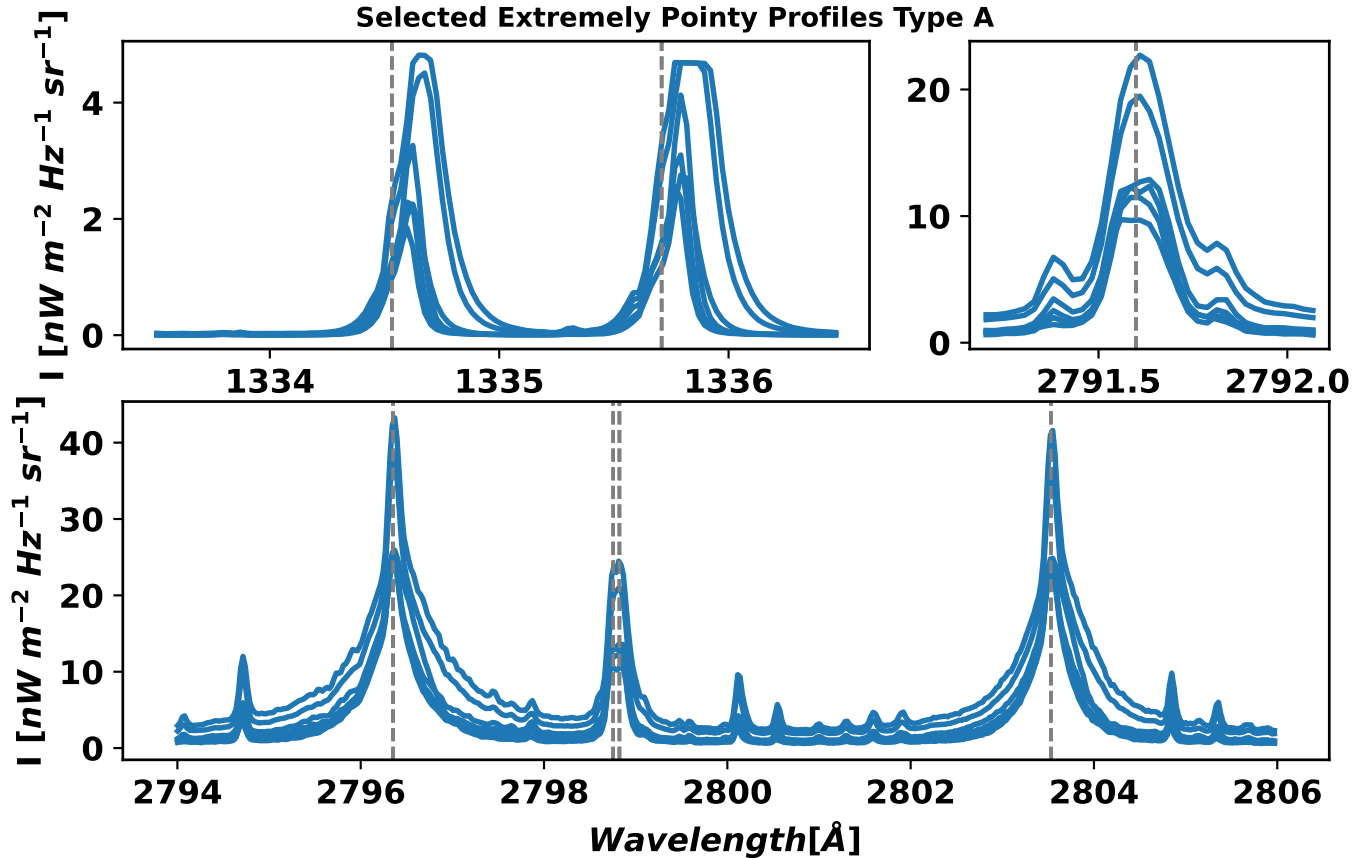
Figure 3. Examples of the type A extremely pointy profiles.

enhanced than the red wing. The Mg II h&k lines are a bit shifted to the red. The Mg II UV triplet lines are clearly shifted to the red, and they have a blue component. Interestingly, the same happens for the C II 1334 & 1335 Å lines.

The last type of profiles seems to be the *combination* of type A and B (see Fig. 5). The main difference is the presence of a well defined blue component, and the peak of the line is now well-centered. Note that the blue component is well distinguished, and the profile can be clearly describe in terms of the $2v, 2r$, and 3 features, that means in terms of 2 peaks and the central depression. In this case, the $2r$ largely dominates over the $2v$ feature, and it is located on the rest spectral position of the line. On the other hand, the 3 feature is present, and it is slightly blue-shifted.

In all the types, the Mg II UV triplet lines show either a blue or red component, or both (see Fig. 3). These components appear, in most of the cases, both in the Mg II UV1 line and the Mg II UV2&3 lines. This behavior indicates that these components are actually belonging to these lines and not to nearby lines in emission.

The spatial distribution of these profiles is shown in the right panel of Figure 2. The Type A profiles are mostly located in the ribbon (dark blue ticks), the type B profiles are located in the leading edge (dark orange ticks), and the combination type profiles are mostly located close to (and just trailing) the leading edge (dark green ticks). The locations displayed in light colors show all the profiles of the various types not shown in Fig. 3, 4 and 5. The profiles associated with these locations have a range of gradually changing appearances within their corresponding type. For instance, a profile in a light blue location is an extremely pointy type A profile but the wings of the Mg II h&k lines look more Lorentzian than Laplacian, in contrast to the most intense ones shown in Fig. 3, which have more Laplacian wings.

The pointy profiles almost always occur in the flare ribbons. Pointy profiles have also been observed during the pre-flare phase, as we have already mentioned. However, it is during the maximum of the flare when the extreme and very pointy profiles appear, as right panel in Fig. 2 shows.

3. RESULTS

Figures 6, 7, 8, and 9 show the results from the inversions of two profiles of type A, and one of type B, and a combination profile, respectively. From top to bottom, from left to right, in each figure, the three first panels show the observed profile (in black dotted line) and the inverted profile (fuch-
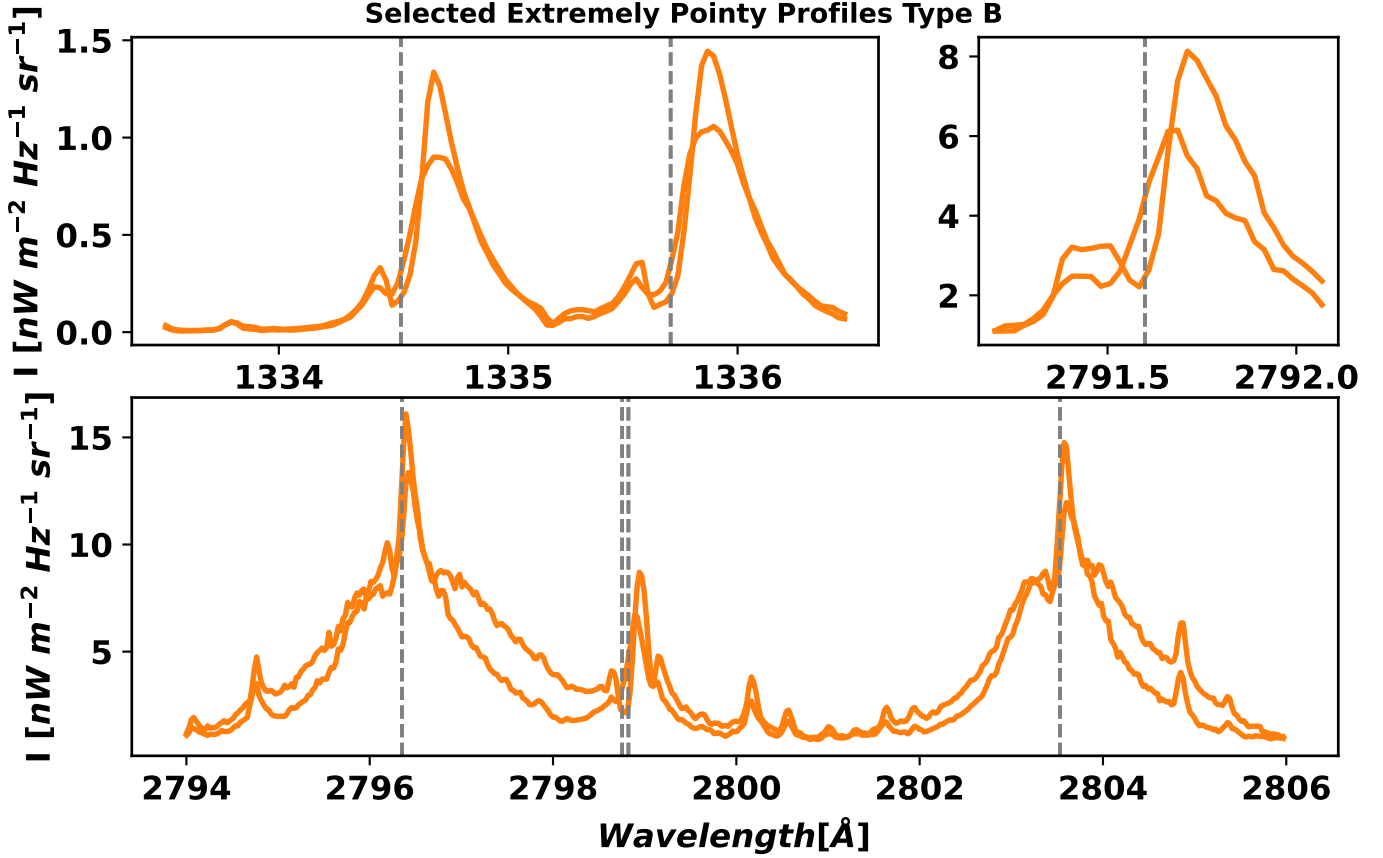
Figure 4. Examples of the type B extremely pointy profiles.

sia) for the C II 1334 & 1335 Å the Mg II UV1, and the Mg II h&k and Mg II UV2&3 lines respectively. In the second row, we also include the inversion for the case that only the Mg II h&k and Mg II UV2&3 lines are inverted (dashed blue)[4]. Thus, we can appreciate the effect of including the C II 1334 & 1335 Å lines (and the Mg II UV1 line) in the inversion to recover the model atmosphere. The two last panels show the T (left panel, left axis, in orange), the n_e (left panel, left axis, in blue), the v_{turb} (left panel, right axis, in green), and the v_{los} (right panel, right axis, in violet). All these values are given with respect to the logarithm of the optical depth, $log(\tau)$[5]. The dashed lines in these panels refer to the thermodynamic parameters corresponding to the Mg II h&k-only inversion. If the dashed blue line is not shown in the Mg II h&k panel (third panel), then the Mg II h&k-onliy inversion failed for the 4th inversion cycle and the model atmosphere shown in the bottom panels correspond to the 3rd cycle.

The fit of the lines in Figure 6, while not perfect, is rather good. Both C II 1334 & 1335 Å lines are well fitted, with the inverted profile capturing the intensity, the shift, the skewness, and fitting the wings relatively well. The fit of the Mg II UV1 is capturing the width of the line, and the intensity, although it is missing the little depression in the core and the little bumps present both in the blue and the red wing. The fit of the Mg II h&k and the Mg II UV2&3 lines is very good for both the multi-line inversion and the Mg II h&k-only inversion. In this case, the fit of the multi-line inversion is better than the Mg II h&k-only inversion. However, that is not always the case (see below). The T shows very large values, between $7.5-20kK$ at $-6.5 < log(\tau) < -6.0$. Given the goodness of the fit both in the C II 1334 & 1335 Å lines and the Mg II h&k lines, it is difficult to argue why such high values would be incorrect. The n_e shows a steady increase from $-6.5 < log(\tau) < -2.5$. The v_{turb} has values $\approx 20km\ s^{-1}$ in the high chromosphere[6] ($log(\tau) = -6$), and a wavy behavior at

---

[4] For the sake of simplicity, since the inversion of the Mg II h&k lines and the Mg II UV2&3 lines are always performed simultaneously, we will refer to this inversion as Mg II h&k-*only inversion*

[5] In this paper, $log(\tau)$ actually means $log_{10}(\tau_{500})$, that means, the reference of the optical depth unity corresponds to the continuum at 500 nm.

[6] Roughly speaking, we define in this paper the high chromosphere as the optical depth range $-6.5 < log(\tau) < -5$, the mid chromosphere is $-5 < log(\tau) < -4$, the low chromosphere is $-4 < log(\tau) < -2$, the high photosphere is $-2 < log(\tau) < -1$, and the low photosphere is $-1 < log(\tau) < 0$.
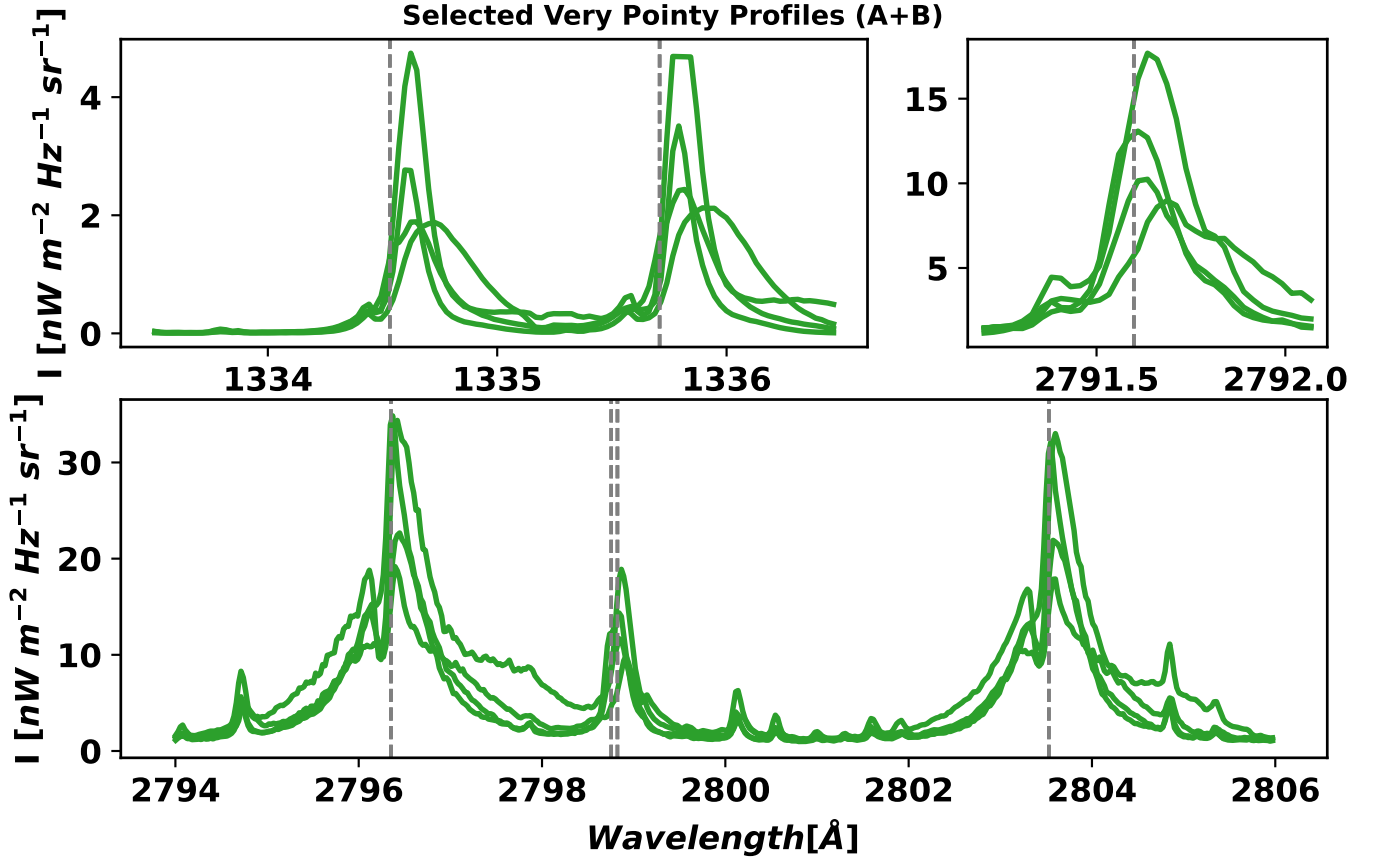
Figure 5. Examples of the combined type of pointy profile.

$-6 < log(\tau) < 0$. The v_{los} shows an important downflow gradient in the high chromosphere, from 0 to +20 $km\ s^{-1}$. Then, from $-6 < log(\tau) < -2$, the v_{los} drops down to 0 $km\ s^{-1}$ in a slightly oscillatory way. At $-2 < log(\tau)$, there is a significant upflow gradient, from 0 to $-20\ km\ s^{-1}$. Figure 7 shows a similar behavior in T and n_e. The v_{turb}, in this case, peaks at $log(\tau)$= -5.6 with a value of $\approx 20\ km\ s^{-1}$. The v_{los} shows a steady downflow that increases from a 0 $km\ s^{-1}$ in the high chromosphere to 20 $km\ s^{-1}$ at $log(\tau)$=-1.8, followed by an upflow up to $-20\ km\ s^{-1}$ in the high-photosphere ($-2 < log(\tau) < -1$). The optical depth where the flow turns from downflow to upflow in both cases is where the minimum of T and the decrease of n_e occurs.

We note that we should not consider the values in the low-photosphere $-1 < log(\tau) < 0$ as realistic, since the photospheric lines available in the IRIS Mg II h&k spectral range do not show such a high Doppler shift. We have tested that the photospheric flows ($-2 < log(\tau)$) shown in the figures of

this paper do not contribute to any aspects of the C II 1334 & 1335 Å lines and the Mg II h&k lines. In some cases, e.g. Figure 9, the velocity flows at $-2 < log(\tau) < -1$ have an impact in the Mg II UV triplet lines. That means, the velocities captured at this optical range are needed to explain the observed profiles, and therefore, despite their large values, considered as feasible.

The values at $log(\tau) < -6.5$ should be taken with caution. This is because the current inversion scheme is not able to capture changes in the thermodynamics - if any - in that optical depth range from the C II 1334 & 1335 Å lines. None of the lines in this study are sensitive to changes in the thermodynamics at $-1 < log(\tau)$. The values shown at these two ranges are due to the interpolation used by the inversion code in the nodes at that optical depths, and we have tested that changing those values in these ranges has no effect on the inverted profiles.

The profiles in Figure 8 show an extremely pointy profile of type B. The T peaks now a bit lower in the chromosphere, at $log(\tau)$= −5, but now the T strikingly decreases from $-7 < log(\tau) < -5$. The T minimum and n_e depression is around $log(\tau) = -1$. Again, it is around that optical depth where the v_{los} changes its sign. There is another significant

---

These ranges are dynamically changing, especially for events such as flares. Throughout such changes, the region just above the temperature minimum is referred to as the low chromosphere, while the steep, large increase of the temperature at small $log(\tau)$ values is the top of the chromosphere.
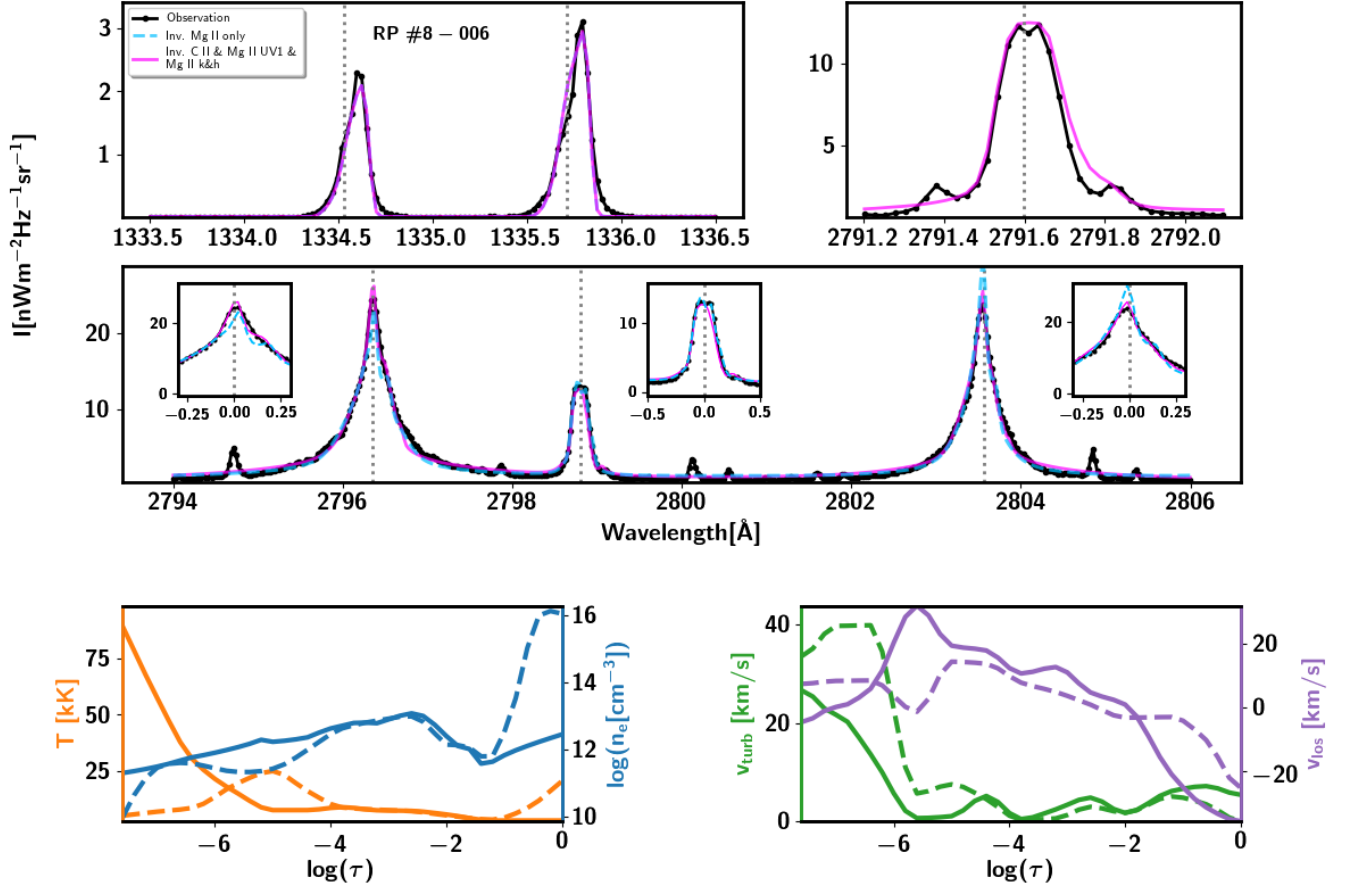
Figure 6. Inversion (fit) of the C II 1334 & 1335 Å, Mg II UV1 Mg II h&k, and Mg II UV2&3 lines of an extremely pointy profile type A, and the model recovered from the inversion. The three first panels show the inversion of an extremely pointy profile type A (in dotted, black line). The dashed, blue line corresponds to the inversion only taking into account the Mg II h&k lines. The fuchsia line corresponds to the inversion considering simultaneously the C II 1334 & 1335 Å lines, the Mg II UV1 line, and the Mg II h&k lines - including the Mg II UV2&3 lines. The last two panels show the thermodynamic variables obtained from the inversions: temperature (T, in orange), logarithm of the electron density (n_e, in blue), velocity of turbulent motions or micro-turbulence (v_{turb}, in green), and line-of-sight velocity (v_{los}, in violet). The dashed lines correspond to model recovered from the inversion considering only the Mg II h&k lines, while the solid lines correspond to the inversion considering all the lines mentioned above.

difference, the flow is now the opposite: there is a decreasing upflow as the optical depth increase from the high chromosphere ($log(\tau)= -6.5$) towards the mid-low chromosphere ($-4 < log(\tau) < -2$), where the v_{los} is around 0 $km\ s^{-1}$. Then a downflow increases as the optical depth increases towards the photosphere. The turbulent motions in the high chromosphere have again a value $\approx -20\ km\ s^{-1}$, being $\approx -10\ km\ s^{-1}$ in the mid chromosphere and the photosphere.

The model atmosphere associated with the profiles of the combined type (see Figure 9) is closer to the one associated to extremely profiles type B than to type A. Thus, the T has a decrease again in the range $-6.5 < log(\tau) < 5.8$, then a peak in $\approx 20kK$, with the minimum of T and n_e around $log(\tau)= -1.5$. The v_{turb} now peaks at $log(\tau)= -5.8$ with a value $\approx 25\ km\ s^{-1}$, then decreases between $-4 < log(\tau) < 3$ to a value of $\approx 5\ km\ s^{-1}$, and peaks at a value of $\approx 10\ km\ s^{-1}$

and 15 $km\ s^{-1}$ for the type B and the combined type respectively at the photosphere, which would explain the large broad wings of the Mg II h&k lines.

3.1. *How the extremely pointy profiles are formed*

A simple way to create an extremely pointy type A profile in the Mg II h&k lines is by considering a extreme gradient in the high chromosphere. Figure 10 shows how to get an extremely pointy profile type A from a double-peaked Mg II h&k profile. The red and blue profiles are the result of considering the T, v_{turb}, and n_e of the double-peaked profile (in grey) with the v_{los} shown in red and blue lines respectively in the bottom, right-most panel of the Figure 10. In this example the steep gradient is located between $-7 < log(\tau) < -5.5$ and goes from ± 50 to $0\ km\ s^{-1}$. We have done several tests and we have also obtained extremely pointy profiles for
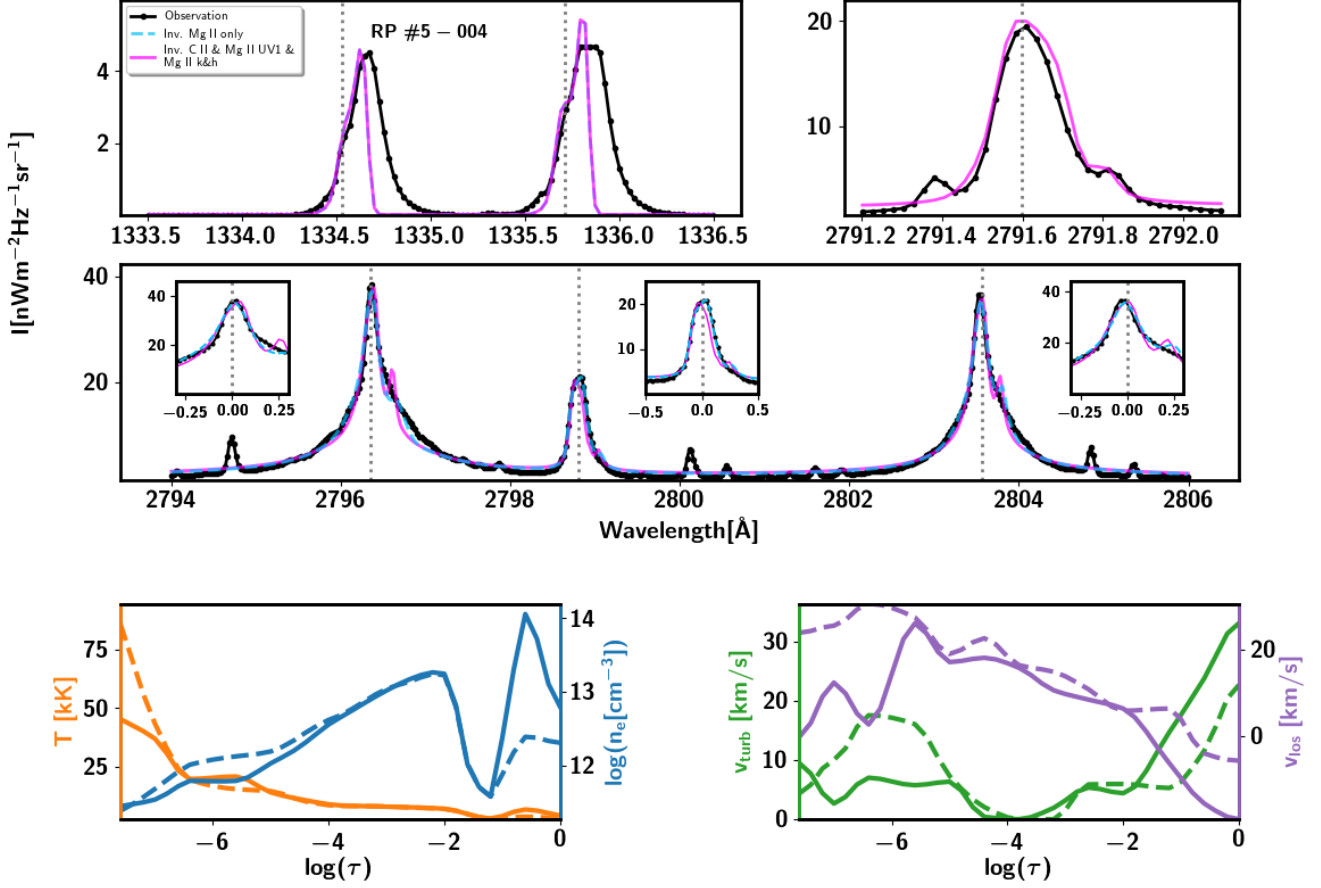
Figure 7. Inversion (fit) of the C II 1334 & 1335 Å, Mg II UV1 Mg II h&k, and Mg II UV2&3 lines of another extremely pointy profile type A, and the model recovered from the inversion. See caption of Figure 6 for details.

lower values of v_{los}. Note that the C II 1334 & 1335 Å lines are shifted to the red and blue wavelengths for the downflow and upflow gradients respectively, and they show the skewness previously observed in the IRIS data.

Another way of studying what can cause pointy profiles is by studying the contribution of v_{los} to the synthetic profile obtained by the inversion of the extremely pointy type A profile shown in Figure 6 (in fuchsia). We have taken the same thermodynamics atmosphere associated with that profile (see bottom panels in the 6) and imposed a zero velocity at all optical depths ($v_{los}(\tau) = 0 \ km \ s^{-1}$), and then synthesized that new atmosphere. Again, we obtain a double-peaked profile shown in Figure 11.

In summary, the extremely pointy shape of these profiles is the signature of an extreme gradient in the v_{los} in the chromosphere. In the context of a flare, the downflows and upflows are associated with the *chromospheric condensation* and *evaporation* respectively. In this case, these flows have extreme gradients along the optical depth and take place in a well-determined optical depth range: the high chromosphere.

4. DISCUSSION

The inversion and interpretation of the profiles presented in this paper entail a significant challenge. The highly dynamic event studied - the maximum of an X1.0-class flare, is reflected both in the associated profiles and the thermodynamics recovered from the inversions of these profiles. The extremely pointy and combined type profiles belong to the same solar feature - the ribbon, including its leading and trailing edge. However, they are related to slightly different stages of the same event, which happen simultaneously in different location in the ribbon. We should understand that both the variation in the appearance of the profiles and their associated thermodynamics is gradual. Thus, while we have focused our attention on the most significant of each type, the following interpretation capture the main physical properties during the maximum of the flare. Figure 12 is particularly helpful for this interpretation.

For the positions scanned by the IRIS slit, the location of the trailing edge of the upper ribbon is at $[X, Y] = [512, 268]$ and in the lower ribbon at $[X, Y] = [517 - 526, 263]$. It is in these locations where the extremely pointy type A profiles such as the ones shown in Fig. 3 are found, while the rest of
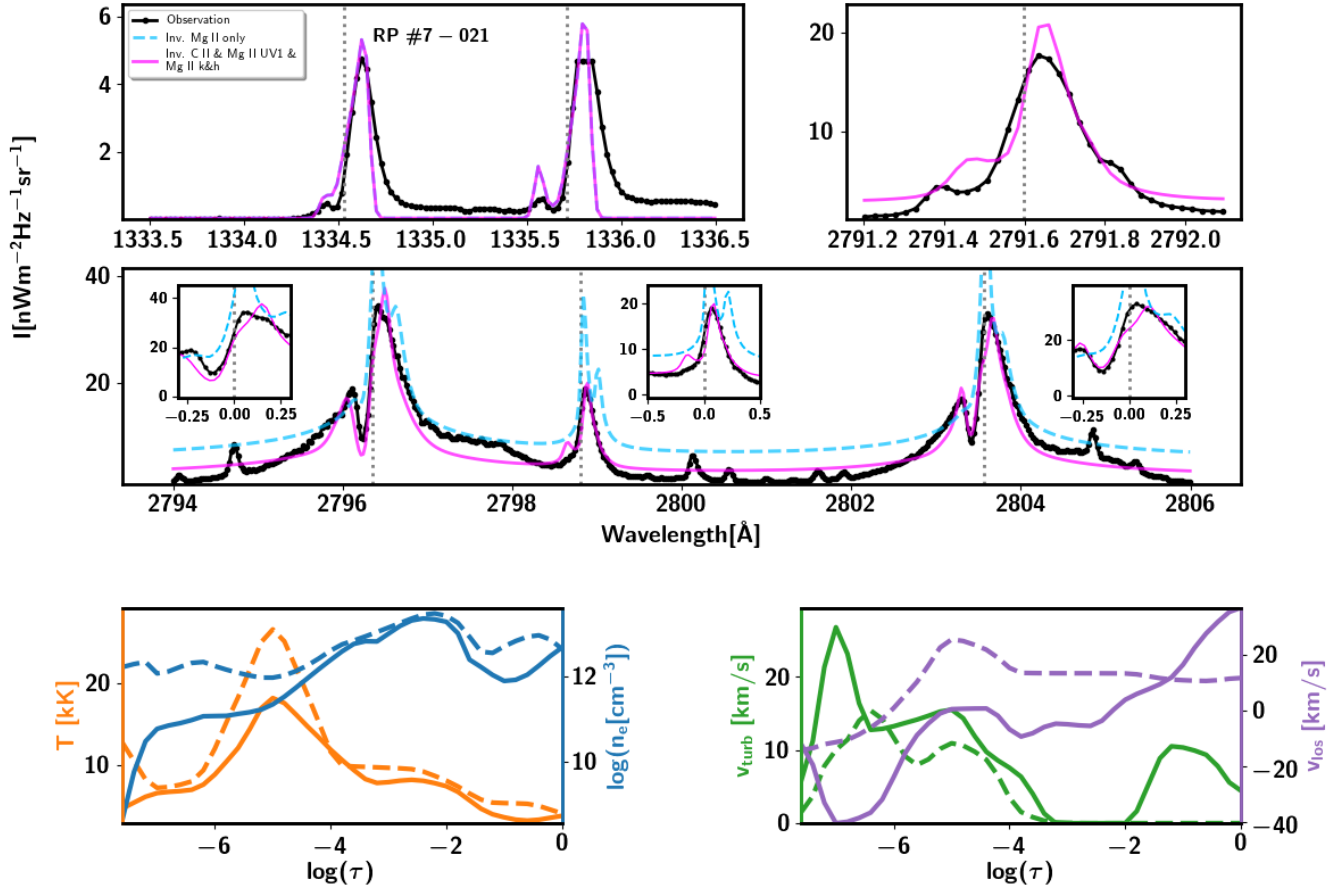
Figure 8. Inversion (fit) of the C II 1334 & 1335 Å, Mg II UV1 Mg II h&k, and Mg II UV2&3 lines of an extremely pointy profile type B, and the model recovered from the inversion. See caption of Figure 6 for details.

the profiles of this type are mostly located within the ribbon itself. The location for the leading edge of the upper ribbon is at $[X,Y] = [512, 277]$ and in the lower ribbon at $[X,Y] = [512 - 526, 257 - 255]$. Most of the type B pointy profiles are located at the leading edge of the lower ribbon, while the combination profiles are located within the ribbon on the trailing side immediately adjacent to the leading edge and the ribbon of the ribbon (some are also located in the region just leading the trailing edge of the ribbon). Thus, as the ribbon is energized, starting from the trailing edge towards the leading edge, the profiles go from extremely pointy type A to the combination type and finally to the type B.

Because ribbons propagate across the solar surface as the flare evolves, the spatial distribution of the thermodynamic parameters from trailing to leading edge of the ribbon provide a window into the typical temporal evolution within a single location. Is is interesting to note that the trailing edge has been energized longer than the leading edge in this single snapshot. That could explain why in these locations the temperature is so high in the high chromosphere ($log(\tau)$= −5.8, first panel in the first row of Fig. 12), while in the rest of

the ribbon the high chromosphere temperature is lower. The trailing edge also differs from the rest of the ribbon when we consider the temperature difference between the high and middle chromosphere. In the trailing edge the temperature of the high chromosphere is higher than in the mid chromosphere. In contrast, the mid chromosphere temperature ($log(\tau)$= −4.2, first panel of the second row of Fig. 12) is higher than in the high chromosphere for the leading edge and interior of the ribbon itself. Thus, the bump in the temperature at $log(\tau) \approx -5$ observed in Fig. 8 has not reached yet the high-chromosphere, as it does in Fig. 7 and even higher in Fig. 6. This spatial pattern of a somewhat reduced temperature in the high chromosphere accompanied by an increase in the mid chromosphere is seen in both flare ribbons but most clear in the lower ribbon as IRIS scanned this ribbon more fully. This pattern has been obtained in some numerical models of flare energy deposition in the chromosphere by Allred et al. 2015. These observations support a scenario in which energy is deposited in the middle chromosphere, with associated local temperature increase. This energy deposi-
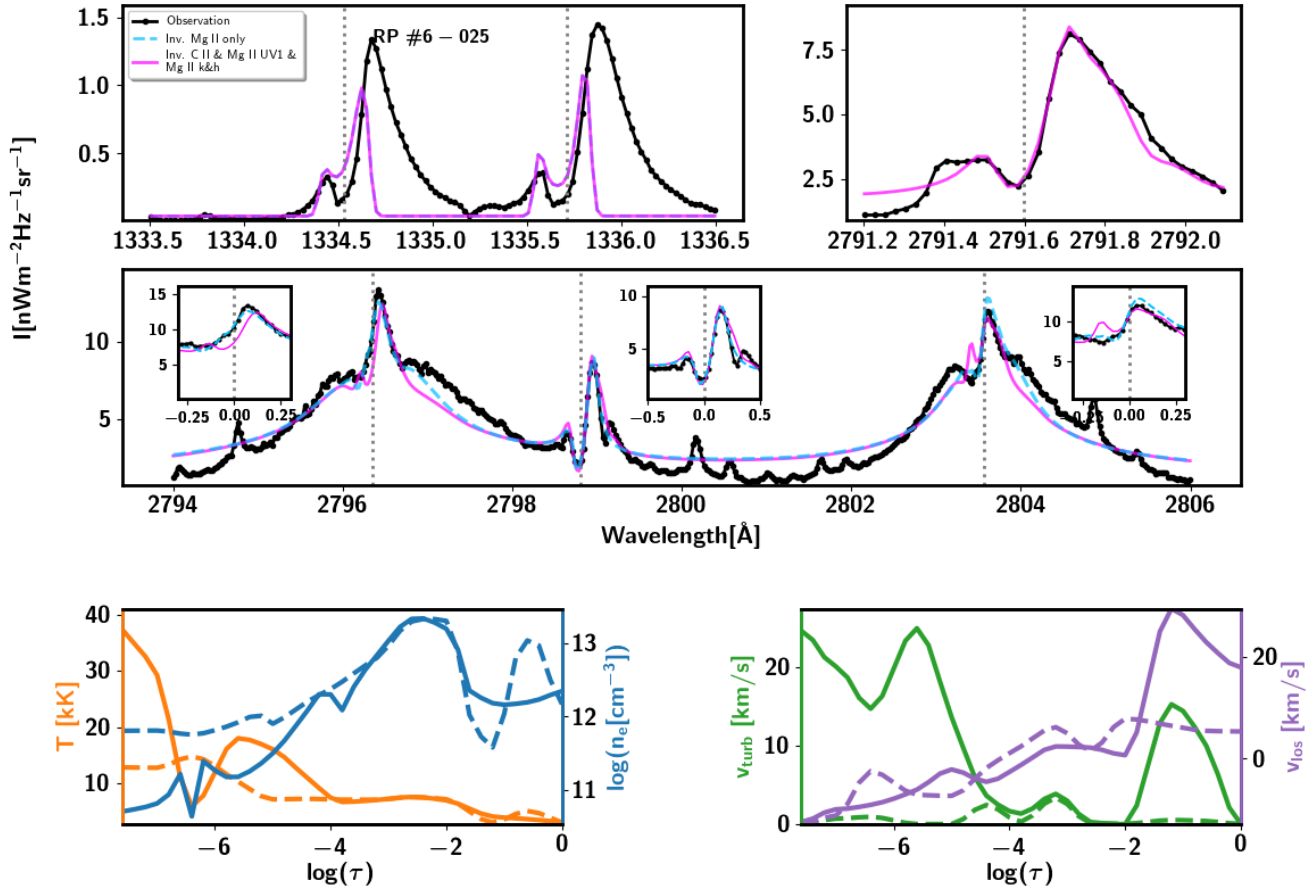
Figure 9. Inversion (fit) of the C II 1334 & 1335 Å, Mg II UV1 Mg II h&k, and Mg II UV2&3 lines of a combined pointy profile type, and the model recovered from the inversion. See caption of Figure 6 for details.
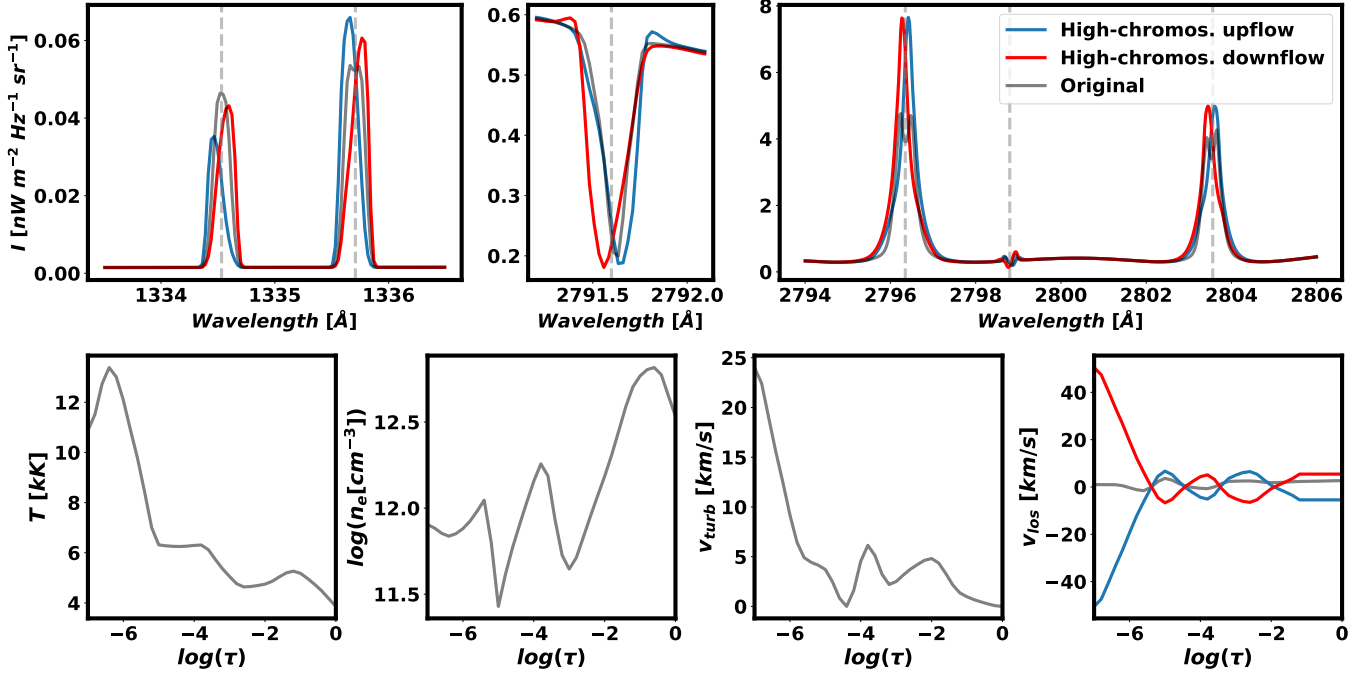
Figure 10. Creating an Mg II h&k extremely pointy profile type A (red or blue) from a double-peaked Mg II h&k profile (grey) by considering an extreme gradient downflow (red) or upflow (blue) in the high chromosphere.
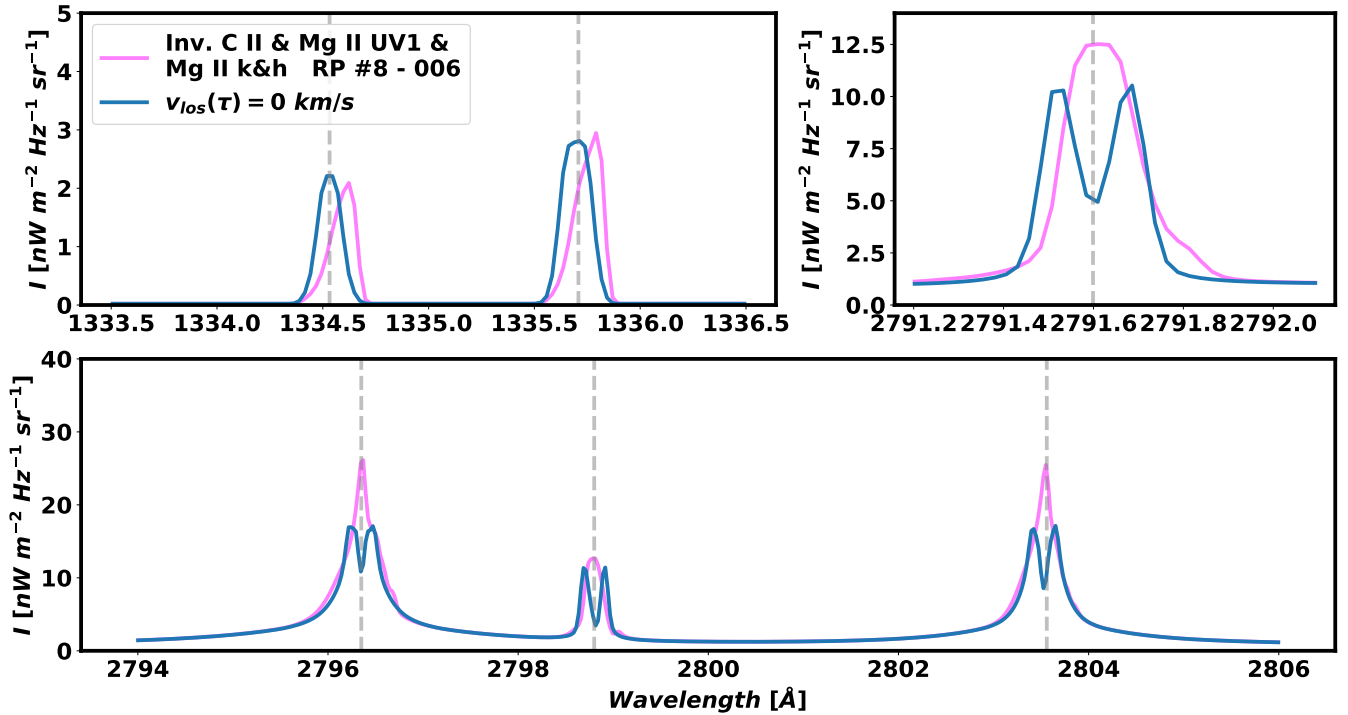

Figure 11. Deconstruction of the synthetic extremely pointy type A profile (in fuchsia) shown in the Figure 6 that shows the role played by the v_{los}. The profile in blues shows the resulting profile by considering v_{los}= 0 $km\ s^{-1}$ in the atmosphere associated to the profile mentioned above (two bottom panels in the Figure 6).
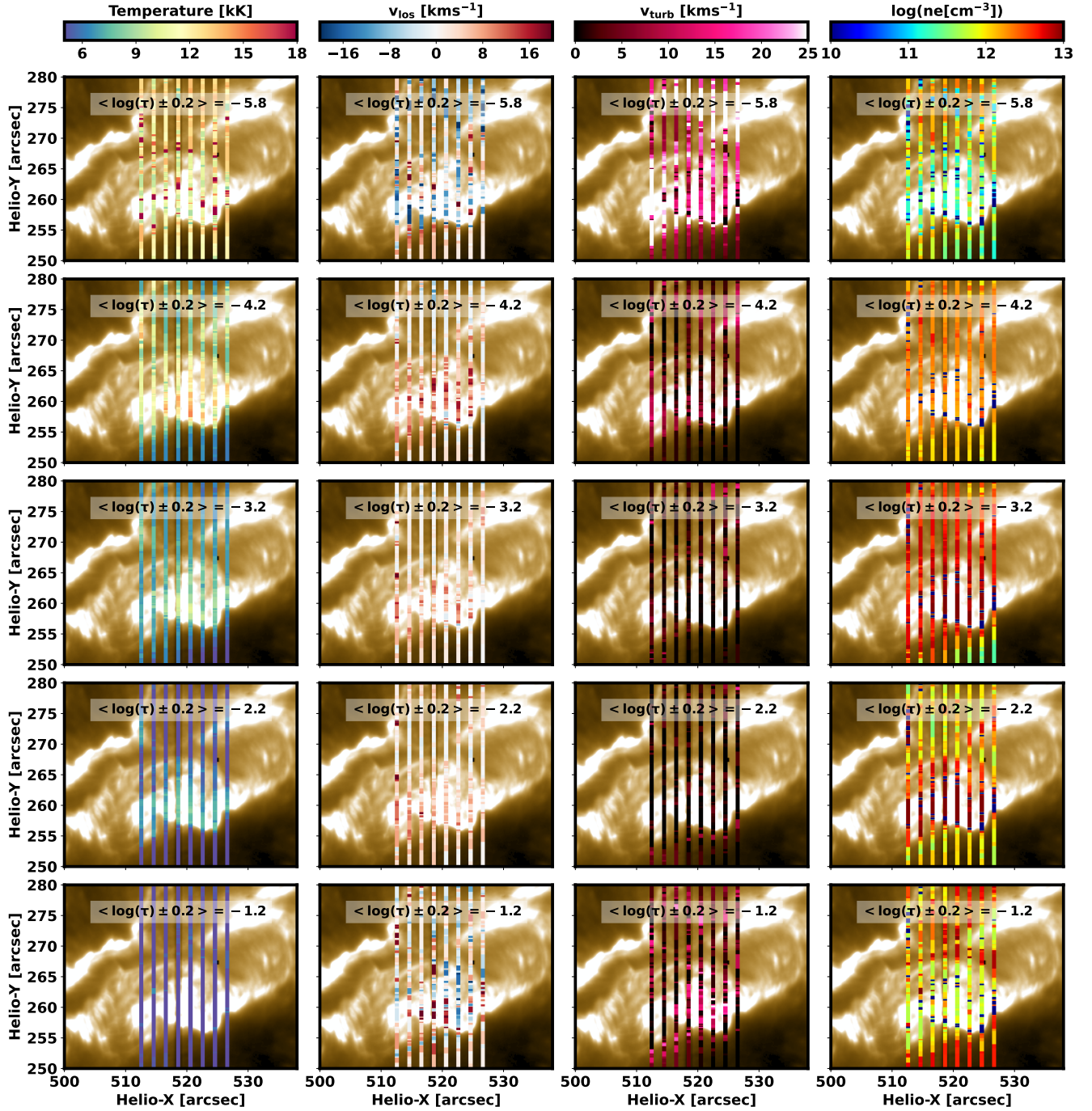
.

Figure 12. Maps of thermodynamic values (columns) during the maximum of the X1.0-class flare SOL2014-03-29T17:48, for various optical depths (rows).

tion affects the high chromosphere at later times, as the flare evolves.

The most critical physical parameter that contributes to the very distinctive profiles studied in this paper is the line-of-sight velocity. As we have demonstrated, the extremely pointy profiles of the Mg II h&k lines, but also of the C II 1334 & 1335 Å lines, need the presence of a strong, divergent velocity gradient located between the high and middle chromosphere. In addition, the Mg II UV triplet lines have signatures associated with strong velocities in the high photosphere. The divergent flow located between the high- and mid-chromosphere can be appreciated between the first (i.e., top) and the second panel of the second column of Fig. 12. There, we can observe predominantly an upflow in the ribbon in the high chromosphere ($log(\tau)$= −5.8), while in the middle chromosphere and lower regions in the atmosphere ($-4.2 < log(\tau)$) the ribbon shows a downflow. Note that in the trailing edge, there are some locations where the velocities in the high chromosphere are positive, i.e., they host downflows. Again, these locations are likely *ahead in time* (i.e., have evolved for the longest time since the start of the flare), so it is possible they may have experienced the upflows at an earlier stage of their evolution. The presence of a divergent flow is compatible with an scenario where an electron beam propagating downwards from the flare reconnection site in the corona impacts the dense chromosphere (thick-target model, Hudson 1972). Such divergent flows have also been obtained in radiation hydrodynamic experiments by Kerr et al. 2016 and Kowalski et al. 2017 who studied the same flare that we analyzed in the current paper. However, the synthetic Mg II h&k profiles obtained by Kerr et al. 2016 show the k_3 feature in absorption, which indicates that their models are missing some ingredient(s) needed to reproduce the observed profiles. Similarly, the temperature increase where the divergent flows occur in Kowalski et al. 2017 is much higher ($T \approx 10 MK$) than the one we obtain. What can explain the strong velocity flows that we observe in the high photosphere? Several results suggest that these can be explained by the different penetration of the different energy regimes of the electron beams. Graham et al. 2020 demonstrated that low-energy electrons ($E \approx 25-50\ keV$) are responsible for the evaporation-condensation in the high chromosphere, while very high-energy electrons ($E \geq 50\ keV$) can penetrate deeper in the atmosphere and produce a similar situation in the high photosphere. These authors used, in addition to the Mg II UV1 line, the optically thin lines Fe I 2814.11 Å, and Fe II 2813.3 and 2814.45 Å. In their study all these lines show a strong red component. However, in the flare we study here no red components are present in the Fe I and Fe II lines, and the Mg II UV1 line shows on occasions a strong red component, but also a blue and red components in other cases. Likely, the situation shown in

Fig. 12 is compatible with the scenario described by Graham et al. 2020 and the one previously suggested by Libbrecht et al. 2019 (see Fig. 14 of their paper). Here, in agreement with Graham et al. 2020, we interpret that the bounce back motion that Libbrecht et al. 2019 locates in the chromosphere is lower in our case, reaching the high-photosphere. In summary, there are two slabs, one located between the high- and mid-chromosphere and the other in the high photosphere, that are suffering the impact from energized electron coming from the corona, and producing explosive, divergent upflows and downflows. These slabs are not necessary located in the same feature of the ribbon at the same time, and their location evolves as the ribbon is energized by the flare.

Finally, the turbulent motions are rather strong in the high and middle chromosphere in the ribbons. It is in these regions where the core of both the C II 1334 & 1335 Å lines and the Mg II h&k lines is sensitive to this parameter. Therefore these values are rather feasible. In the low chromosphere and the high photosphere the v_{turb} in the ribbons is negligible. The extended, broad wings of the Mg II h&k are sensitive to changes in v_{turb} in the mid chromosphere, while the Mg II UV triplet lines are sensitive to turbulence in the low chromosphere. We also note that the electron density in the ribbons is $12 < \log(n_e) < 13$ in the chromosphere, reaches its maximum in the low chromosphere with a value of $\log(n_e) \approx 15$, just before the temperature minimum, which is *pushed down* (in log *tau* terms) towards the low-photosphere ($log(\tau) \approx -1$).

The spectral profiles studied in this article are challenging to model and interpret due to the complexity of the physical conditions that generates them. In addition to belonging to an extreme event (an X1-class flare), we note that several physical processes such as upflows and downflows, or heating and cooling, occur simultaneously in the same structure - the ribbon. We are analyzing the maximum of the flare, but that does not mean all regions in the ribbon show the same behavior. For example, the trailing edge experiences different physical conditions than the ribbon itself. The interpretation of the peculiar profiles clearly will depend on where and when they are observed in the macroscopic spatio-temporal evolution of the flare. Until now there have not been any theoretical or numerical models that are able to properly reproduce these profiles. In this context, our investigation and results provide strict observational constraints to these models, and suggest a reasonable physical scenario.

CONFLICT OF INTEREST STATEMENT

AUTHOR CONTRIBUTIONS

This paper has been led by ASD. He has made the analysis of the IRIS spectra, and the interpretation of the inver-

sions and the models recovered from them, as well as the main contain of the manuscript . BDP has contributed with meaningful ideas, enlightening discussions with ASD, and with critical comments and improvements to the manuscript. Both authors have reviewed this manuscript and approved it for publication.

DATA AVAILABILITY STATEMENT

The original datasets used in this investigations are available in a publicly accessible repository. They can be found here, or through the IRIS L2 data search tool (https://iris.lmsal.com/search/).

REFERENCES

Allred, J. C., Kowalski, A. F., and Carlsson, M. (2015). A Unified Computational Model for Solar and Stellar Flares. *ApJ* 809, 104. doi:10.1088/0004-637X/809/1/104

Carlsson, M., Leenaarts, J., and De Pontieu, B. (2015). What Do IRIS Observations of Mg II k Tell Us about the Solar Plage Chromosphere? *ApJL* 809, L30. doi:10.1088/2041-8205/809/2/L30

Carlsson, M. and Stein, R. F. (1995). Does a Nonmagnetic Solar Chromosphere Exist? *ApJL* 440, L29. doi:10.1086/187753

Carlsson, M. and Stein, R. F. (1997). Formation of Solar Calcium H and K Bright Grains. *ApJ* 481, 500–514. doi:10.1086/304043

de la Cruz Rodríguez, J., Leenaarts, J., and Asensio Ramos, A. (2016). Non-LTE Inversions of the Mg II h & k and UV Triplet Lines. *ApJL* 830, L30. doi:10.3847/2041-8205/830/2/L30

de la Cruz Rodríguez, J., Leenaarts, J., Danilovic, S., and Uitenbroek, H. (2019). STiC: A multiatom non-LTE PRD inversion code for full-Stokes solar observations. *A&A* 623, A74. doi:10.1051/0004-6361/201834464

De Pontieu, B., Title, A. M., Lemen, J. R., Kushner, G. D., Akin, D. J., Allard, B., et al. (2014). The Interface Region Imaging Spectrograph (IRIS). *SoPh* 289, 2733–2779. doi:10.1007/s11207-014-0485-y

del Pino Alemán, T., Casini, R., and Manso Sainz, R. (2016). Magnetic Diagnostics of the Solar Chromosphere with the Mg II h-k Lines. *ApJL* 830, L24. doi:10.3847/2041-8205/830/2/L24

Dimitrijević, M. S. and Sahal-Bréchot, S. (1995). Stark broadening parameter tables for Mg II. *Bulletin Astronomique de Belgrade* 151, 101–114

Dimitrijević, M. S. and Sahal-Bréchot, S. (1998). Electron-Impact Broadening of MgII Spectral Lines for Astrophysical and Laboratory Plasma Research. *PhyS* 58, 61–71. doi:10.1088/0031-8949/58/1/009

Feldman, U. and Doschek, G. A. (1977). The 3s-3p and 3p-3d lines of Mg II observed above the solar limb from Skylab. *ApJL* 212, L147–L150. doi:10.1086/182395

Graham, D. R., Cauzzi, G., Zangrilli, L., Kowalski, A., Simões, P., and Allred, J. (2020). Spectral Signatures of Chromospheric Condensation in a Major Solar Flare. *ApJ* 895, 6. doi:10.3847/1538-4357/ab88ad

Hudson, H. S. (1972). Thick-Target Processes and White-Light Flares. *SoPh* 24, 414–428. doi:10.1007/BF00153384

Jefferies, J. T. (1968). *Spectral line formation*

Kaiser, M. L., Kucera, T. A., Davila, J. M., St. Cyr, O. C., Guhathakurta, M., and Christian, E. (2008). The STEREO Mission: An Introduction. *SSRv* 136, 5–16. doi:10.1007/s11214-007-9277-0

Kerr, G. S., Fletcher, L., Russell, A. J. B., and Allred, J. C. (2016). Simulations of the Mg II k and Ca II 8542 lines from an AlfvÉn Wave-heated Flare Chromosphere. *ApJ* 827, 101. doi:10.3847/0004-637X/827/2/101

Kerr, G. S., Simões, P. J. A., Qiu, J., and Fletcher, L. (2015). IRIS observations of the Mg ii h and k lines during a solar flare. *A&A* 582, A50. doi:10.1051/0004-6361/201526128

Kleint, L., Battaglia, M., Reardon, K., Sainz Dalda, A., Young, P. R., and Krucker, S. (2015). The Fast Filament Eruption Leading to the X-flare on 2014 March 29. *ApJ* 806, 9. doi:10.1088/0004-637X/806/1/9

Kneer, F., Scharmer, G., Mattig, W., Wyller, A., Artzner, G., Lemaire, P., et al. (1981). OSO-8 Observations of CAII H and K MGII H and K Lyman-Alpha and Lyman-Beta above a Sunspot. *SoPh* 69, 289–300. doi:10.1007/BF00149995

Kohl, J. L. and Parkinson, W. H. (1976). The Mg II h and k lines. I. Absolute center and limb measurements of the solar profiles. *ApJ* 205, 599–611. doi:10.1086/154317

Kosugi, T., Matsuzaki, K., Sakao, T., Shimizu, T., Sone, Y., Tachikawa, S., et al. (2007). The Hinode (Solar-B) Mission: An Overview. *SoPh* 243, 3–17. doi:10.1007/s11207-007-9014-6

Kowalski, A. F., Allred, J. C., Daw, A., Cauzzi, G., and Carlsson, M. (2017). The Atmospheric Response to High Nonthermal Electron Beam Fluxes in Solar Flares. I. Modeling the Brightest NUV Footpoints in the X1 Solar Flare of 2014 March 29. *ApJ* 836, 12. doi:10.3847/1538-4357/836/1/12

Leenaarts, J., Pereira, T. M. D., Carlsson, M., Uitenbroek, H., and De Pontieu, B. (2013a). The Formation of IRIS Diagnostics. I. A Quintessential Model Atom of Mg II and General Formation Properties of the Mg II h&k Lines. *ApJ* 772, 89. doi:10.1088/0004-637X/772/2/89

Leenaarts, J., Pereira, T. M. D., Carlsson, M., Uitenbroek, H., and De Pontieu, B. (2013b). The Formation of IRIS Diagnostics. II. The Formation of the Mg II h&k Lines in the Solar Atmosphere. *ApJ* 772, 90. doi:10.1088/0004-637X/772/2/90

Lemaire, P., Choucq-Bruston, M., and Vial, J. C. (1984). Simultaneous H and K Ca ii, h and k Mg ii, Lα and Lβ H i profiles of the April 15, 1978 solar flare observed with the OSO-8/L.P.S.P. experiment. *SoPh* 90, 63–82. doi:10.1007/BF00153785

Lemaire, P. and Gouttebroze, P. (1983). Magnesium II line formation - The contribution of high atomic levels to the resonance lines. *A&A* 125, 241–245

Lemaire, P. and Skumanich, A. (1973). Magnesium II Doublet Profiles of Chromospheric Inhomogeneities at the Center of the Solar Disk. *A&A* 22, 61

Libbrecht, T., de la Cruz Rodríguez, J., Danilovic, S., Leenaarts, J., and Pazira, H. (2019). Chromospheric condensations and magnetic field in a C3.6-class flare studied via He I D$_3$ spectro-polarimetry. *A&A* 621, A35. doi:10.1051/0004-6361/201833610

Lin, R. P., Dennis, B. R., Hurford, G. J., Smith, D. M., Zehnder, A., Harvey, P. R., et al. (2002). The Reuven Ramaty High-Energy Solar Spectroscopic Imager (RHESSI). *SoPh* 210, 3–32. doi:10.1023/A:1022428818870

Lites, B. W. and Skumanich, A. (1982). A model of a sunspot chromosphere based on OSO 8 observations. *ApJS* 49, 293–315. doi:10.1086/190800

Liu, W., Heinzel, P., Kleint, L., and Kašparová, J. (2015). Mg II Lines Observed During the X-class Flare on 29 March 2014 by the Interface Region Imaging Spectrograph. *SoPh* 290, 3525–3543. doi:10.1007/s11207-015-0814-9

MacQueen, J. (1967). . In *Fifth Berkeley Sympos. Math. Statist. and Probability. I: Statistics*, ed. C. University California Press, Berkeley. 281

Manso Sainz, R., del Pino Alemán, T., Casini, R., and McIntosh, S. (2019). Spectropolarimetry of the Solar Mg II h and k Lines. *ApJL* 883, L30. doi:10.3847/2041-8213/ab412c

Panos, B., Kleint, L., Huwyler, C., Krucker, S., Melchior, M., Ullmann, D., et al. (2018). Identifying Typical Mg II Flare Spectra Using Machine Learning. *ApJ* 861, 62. doi:10.3847/1538-4357/aac779

Panos, B., Kleint, L., and Voloshynovskiy, S. (2021). Exploring Mutual Information between IRIS Spectral Lines. I. Correlations between Spectral Lines during Solar Flares and within the Quiet Sun. *ApJ* 912, 121. doi:10.3847/1538-4357/abf11b

Pereira, T. M. D., Carlsson, M., De Pontieu, B., and Hansteen, V. (2015). The Formation of IRIS Diagnostics. IV. The Mg II Triplet Lines as a New Diagnostic for Lower Chromospheric Heating. *ApJ* 806, 14. doi:10.1088/0004-637X/806/1/14

Pereira, T. M. D., Leenaarts, J., De Pontieu, B., Carlsson, M., and Uitenbroek, H. (2013). The Formation of IRIS Diagnostics. III. Near-ultraviolet Spectra and Images. *ApJ* 778, 143. doi:10.1088/0004-637X/778/2/143

Pereira, T. M. D. and Uitenbroek, H. (2015). RH 1.5D: a massively parallel code for multi-level radiative transfer with partial frequency redistribution and Zeeman polarisation. *A&A* 574, A3. doi:10.1051/0004-6361/201424785

Pesnell, W. D., Thompson, B. J., and Chamberlin, P. C. (2012). The Solar Dynamics Observatory (SDO). *SoPh* 275, 3–15. doi:10.1007/s11207-011-9841-3

Rathore, B., Carlsson, M., Leenaarts, J., and De Pontieu, B. (2015). The Formation of IRIS Diagnostics. VI. The Diagnostic Potential of the C II Lines at 133.5 nm in the Solar Atmosphere. *ApJ* 811, 81. doi:10.1088/0004-637X/811/2/81

Rubio da Costa, F. and Kleint, L. (2017). A Parameter Study for Modeling Mg II h and k Emission during Solar Flares. *ApJ* 842, 82. doi:10.3847/1538-4357/aa6eaf

Rubio da Costa, F., Kleint, L., Petrosian, V., Liu, W., and Allred, J. C. (2016). Data-driven Radiative Hydrodynamic Modeling of the 2014 March 29 X1.0 Solar Flare. *ApJ* 827, 38. doi:10.3847/0004-637X/827/1/38

Sainz Dalda, A., de la Cruz Rodríguez, J., De Pontieu, B., and Gošić, M. (2019). Recovering Thermodynamics from Spectral Profiles observed by IRIS: A Machine and Deep Learning Approach. *ApJL* 875, L18. doi:10.3847/2041-8213/ab15d9

Sánchez Almeida, J. and Lites, B. W. (2000). Physical Properties of the Solar Magnetic Photosphere under the MISMA Hypothesis. II. Network and Internetwork Fields at the Disk Center. *ApJ* 532, 1215–1229. doi:10.1086/308603

Steinhaus, H. (1957). Sur la division des corps matériels en parties. *Bull. Acad. Polon. Sci.* 4, 801

Sukhorukov, A. V. and Leenaarts, J. (2017). Partial redistribution in 3D non-LTE radiative transfer in solar-atmosphere models. *A&A* 597, A46. doi:10.1051/0004-6361/201629086

Thorndike, R. L. (1953). Who belongs in the family? *Psychometrika* 18, 267–276. doi:10.1007/BF02289263

Uitenbroek, H. (1997). THE SOLAR Mg II h AND k LINES - Observations and Radiative Transfer Modeling. *SoPh* 172, 109–116. doi:10.1023/A:1004981412889

Uitenbroek, H. (2001). Multilevel Radiative Transfer with Partial Frequency Redistribution. *ApJ* 557, 389–398. doi:10.1086/321659

Woods, M. M., Sainz Dalda, A., and De Pontieu, B. (2021). Unsupervised Machine Learning for the Identification of Preflare Spectroscopic Signatures. *ApJ* 922, 137. doi:10.3847/1538-4357/ac2667

Xu, Y., Cao, W., Ding, M., Kleint, L., Su, J., Liu, C., et al. (2016). Ultra-narrow Negative Flare Front Observed in Helium-10830 A Using the 1.6 m New Solar Telescope. *ApJ* 819, 89. doi:10.3847/0004-637X/819/2/89

Zhu, Y., Kowalski, A. F., Tian, H., Uitenbroek, H., Carlsson, M., and Allred, J. C. (2019). Modeling Mg II h, k and Triplet Lines at Solar Flare Ribbons. *ApJ* 879, 19. doi:10.3847/1538-4357/ab2238